Reversed-engineered human alveolar lung-on-a-chip model

Di Huang[a,b,1], Tingting Liu[a,b,c,1], Junlong Liao[a,d,1], Sushila Maharjan[a,1], Xin Xie[a], Montserrat Pérez[a,e], Ingrid Anaya[a,e], Shiwei Wang[a], Alan Tirado Mayer[a,f], Zhixin Kang[a], Weijia Kong[a], Valerio Luca Mainardi[a,g,h], Carlos Ezio Garciamendez-Mijares[a,f], Germán García Martínez[a,f], Matteo Moretti[g,i,j], Weijia Zhang[k,l,m], Zhongze Gu[d], Amir M. Ghaemmaghami[n], and Yu Shrike Zhang[a,2]

[a]Division of Engineering in Medicine, Department of Medicine, Brigham and Women's Hospital, Harvard Medical School, Cambridge, MA 02139; [b]Research Center for Nano-Biomaterials & Regenerative Medicine, Department of Biomedical Engineering, College of Biomedical Engineering, Taiyuan University of Technology, Taiyuan, Shanxi 030024, People's Republic of China; [c]Department of Laboratory Diagnosis, The 971th Hospital, Qingdao 266072, People's Republic of China; [d]State Key Laboratory of Bioelectronics, School of Biological Science and Medical Engineering, Southeast University, Nanjing 210096, People's Republic of China; [e]Department of Biotechnological Engineering, Monterrey Institute of Technology and Higher Education, Monterrey, Nuevo León 64849, Mexico; [f]Department of Mechatronics Engineering, Monterrey Institute of Technology and Higher Education, Monterrey, Nuevo León 64849, Mexico; [g]Regenerative Medicine Technologies Lab, Ente Ospedaliero Cantonale, Lugano 6900, Switzerland; [h]Laboratory of Biological Structures Mechanics, Department of Chemistry, Materials and Chemical Engineering Giulio Natta, Politecnico di Milano, 20133 Milano, Italy; [i]Cell and Tissue Engineering Laboratory, IRCCS Istituto Ortopedico Galeazzi, 20161 Milano, Italy; [j]Faculty of Biomedical Sciences, Università della Svizzera Italiana, Lugano 6900, Switzerland; [k]Department of Cardiac Surgery and Shanghai Institute of Cardiovascular Diseases, Zhongshan Hospital, Shanghai Medical College, Fudan University, Shanghai 200032, People's Republic of China; [l]Institute of Biomedical Sciences and Department of Systems Biology for Medicine, Shanghai Medical College, Fudan University, Shanghai 200032, People's Republic of China; [m]The State Key Laboratory of Molecular Engineering of Polymers, Fudan University, Shanghai 200438, People's Republic of China; and [n]Immunology and Immuno-Bioengineering Group, School of Life Science, Faculty of Medicine and Health Sciences, University of Nottingham, NG7 2RD Nottingham, United Kingdom

Edited by Joseph M. DeSimone, Stanford University, Stanford, CA, and approved April 2, 2021 (received for review July 30, 2020)

Here, we present a physiologically relevant model of the human pulmonary alveoli. This alveolar lung-on-a-chip platform is composed of a three-dimensional porous hydrogel made of gelatin methacryloyl with an inverse opal structure, bonded to a compartmentalized polydimethylsiloxane chip. The inverse opal hydrogel structure features well-defined, interconnected pores with high similarity to human alveolar sacs. By populating the sacs with primary human alveolar epithelial cells, functional epithelial monolayers are readily formed. Cyclic strain is integrated into the device to allow biomimetic breathing events of the alveolar lung, which, in addition, makes it possible to investigate pathological effects such as those incurred by cigarette smoking and severe acute respiratory syndrome coronavirus 2 pseudoviral infection. Our study demonstrates a unique method for reconstitution of the functional human pulmonary alveoli in vitro, which is anticipated to pave the way for investigating relevant physiological and pathological events in the human distal lung.

alveoli | distal lung | lung-on-a-chip | inverse opal | three-dimensional

The lung, as the major organ of the human respiratory system, is responsible primarily for gas exchanges and thus, directly exposed to the external environment. Lungs are affected by a plethora of pathologies such as asthma (1); chronic obstructive pulmonary disease (COPD) (2); and infections like influenza (3), pneumonia (4), and tuberculosis (5) as well as lung cancer (6). These pathological manifestations make lung failure one of the leading causes of death globally. More recently, this is further exemplified by the coronavirus disease 2019 (COVID-19) pandemic, which has so far killed more than 3 million people worldwide with total confirmed cases of >140 million (7).

The lack of reliable and physiologically relevant animal models for human respiratory diseases has led to a critical issue for new drug development as more than 90% of the preclinical studies performed in animals do not predict the outcome of human clinical trials (8). This has resulted in a lack of progress in drug development in respiratory medicine, with only a handful of new drugs entering clinical use in the last 50 y (9). In addition, many of the existing cell culture-based models do not replicate the key biological aspects of the human lung and do not adequately reflect the host responses. These models range from simple two-dimensional (2D) cultures of lung cells on polymeric or elastomeric membrane systems to the complex biomimetic lung-on-a-chip microdevices (10). While each of these more complex models (10–14) may have advantages over 2D single-cell cultures, collectively they suffer from important limitations such as use of synthetic polymer membranes with nonphysiological stiffness to culture cells and/or lack of mechanical stimulation (inhalation/exhalation process).

In fact, there is increasing acceptance that the composition and topography of the extracellular matrix (ECM) have major influences on cell functions (15) and regulate cellular responses to various stimuli. As such, ECM features are too critical to be ignored in the design and fabrication of any biologically relevant tissue and disease models. Therefore, there is a clear need for an advanced model system that not only mimics the human lung tissue structurally but also, captures its ECM physiology that is

Significance

This work reports the development of a physiologically relevant human alveolar lung-on-a-chip model, composed of a three-dimensional (3D) porous hydrogel made of gelatin methacryloyl (GelMA) featuring an inverse opal structure, bonded to a compartmentalized chip device that provides air–liquid interface and cyclic breathing motions. Significantly, this GelMA structure has a high similarity to native human alveolar sacs in that they both possess sac-like pores and interconnecting windows between the sacs, in addition to a stiffness similar to the native human distal lung. We showed through multiscale analyses that our 3D GelMA inverse opal structure was better able to maintain the functions of primary human alveolar epithelial cells in a more in vivo-like manner compared with planar models.

Author contributions: D.H., T.L., J.L., S.M., X.X., M.P., I.A., A.M.G., and Y.S.Z. designed research; D.H., T.L., J.L., S.M., X.X., M.P., I.A., S.W., A.T.M., Z.K., W.K., V.L.M., C.E.G.-M., G.G.M., M.M., and Y.S.Z. performed research; D.H., T.L., J.L., S.M., W.Z., Z.G., and Y.S.Z. analyzed data; Y.S.Z. conceptualized the project; and D.H., T.L., J.L., S.M., and Y.S.Z. wrote the paper.

The authors declare no competing interest.

This article is a PNAS Direct Submission.

[1]D.H., T.L., J.L., and S.M. contributed equally to this work.

[2]To whom correspondence may be addressed. Email: yszhang@research.bwh.harvard.edu.

This article contains supporting information online at https://www.pnas.org/lookup/suppl/doi:10.1073/pnas.2016146118/-/DCSupplemental.

Published May 3, 2021.

essential to their functional reproduction in vitro. More importantly, there are no satisfactory models of the distal lung (i.e., the alveolar space) that truly reflect the sac shape anatomy (16–18) to study physiology and pathophysiology. A recent work attempted to develop such a model with bioprinting (19); however, this model merely reflected alveoli's gross anatomy, albeit in much larger scales than the actual features of the human alveoli (millimeters vs. micrometers), and the material used was still incompatible to native tissue in terms of bioactivity.

To address these challenges, herein we report the development of a physiological human-based model that successfully reconstructs the microstructure, ECM properties, air–cell interface, and the breathing events of the pulmonary alveoli, which are the basic units enabling gas exchanges in the human lung. This model, termed as the "alveolar lung-on-a-chip," is composed of a three-dimensional (3D) porous hydrogel made of low-stiffness gelatin methacryloyl (GelMA) featuring an inverse opal structure, bonded to a compartmentalized polydimethylsiloxane (PDMS) chip device that provides the medium supply, the air–liquid interface (ALI), and the cyclic mechanical movements (Fig. 1).

Importantly, the GelMA inverse opal structure has a high similarity to the native human alveolar sacs in that they possess both the sac-like pores and the interconnecting windows between the sacs, in addition to a stiffness close to the native human lung. Due to its 3D nature, it is possible to construct ~7,050 alveoli within an $8 \times 10 \times 3\text{-mm}^3$ model to allow faithful physiological emulation. Primary human alveolar epithelial cells (hAECs) were populated on the surfaces of the sacs to form the monolayer epithelium. The alveolar lung model was further subjected to cyclic inhalation/exhalation movements, as well as used to investigate the effects of cigarette smoke and severe acute respiratory syndrome coronavirus 2 (SARS-CoV-2) pseudoviral infection. Our study provides a unique method for reconstitution of functional alveolar lung-on-a-chip in vitro, potentially paving the way for investigating a range of pathophysiology of the human distal lung, such as infectious diseases affecting the alveolar space including COVID-19.

Results and Discussion

Fabrication of the Alveoli-Like 3D Porous Structure and Formation of the Alveolar Epithelium. The typical process for the fabrication of the alveoli-like 3D GelMA inverse opal structure is schematically presented in Fig. 2 *A*, *i*, where the corresponding optical micrographs are shown in Fig. 2 *A*, *ii*. This process largely follows those published by us (20–24) and others (25–28) with modifications. First, alginate microbeads with a uniform size (201 ± 12 μm) were assembled into a cubic close-packed lattice. Then, 7% GelMA solution was infiltrated into the void spaces of the lattice and cross-linked. Finally, after the removal of the alginate microbeads by the 0.01 M ethylene diamine tetraacetic acid disodium (EDTA) solution, an alveoli-like 3D hydrogel with uniform pores and connecting windows was formed. Very limited amount of GelMA solution was able to infiltrate the contact areas between the microbeads prior to their removal, allowing also formation of interconnecting windows between most, if not all, of the adjacent pores to enable effective ventilation.

Further, 7% GelMA was chosen since it allowed sufficient stability of the resulting sac-like structures while having a stiffness close to the normal lung tissue (29). GelMA was used as the model ECM to fabricate the scaffold due to its biocompatibility, photocross-linkability, availability, and cost-effectiveness (30). Importantly, GelMA possesses some of the essential properties of ECM such as presence of arginine-glycine-aspartic acid sequences, which promote cell attachment, and matrix metalloproteinase-responsive peptide motifs, thus allowing cells to proliferate and spread in/on GelMA-based scaffolds. A range of Young's modulus values has been reported for the human lung tissue depending on the anatomical compartments of the lung and the mechanical testing techniques used, from ~1.4 to 7.2 kPa (31, 32). The compressive modulus of our GelMA hydrogels (double cross-linked; first with Irgacure 2959 and then with microbial transglutaminase [mTG]) was found to be 6.23 ± 0.64 kPa (*SI Appendix*, Fig. S1), which is within the range of the mechanical strengths reported for the native lung tissue. In addition, the swelling ratios of the GelMA hydrogels (double cross-linked) were significantly smaller (~8 and ~10% for 2D and 3D GelMA hydrogels, respectively) than those photocross-linked with Irgacure 2959 alone (~12 and ~15% for 2D and 3D GelMA hydrogels, respectively), as shown in *SI Appendix*, Fig. S2*A*. Thus, we first photocross-linked our GelMA constructs using Irgacure 2959 and then further chemically cross-linked them using mTG to increase their stability as we have shown also in the degradation profiles in *SI Appendix*, Fig. S2*B*. We have further used collagen methacryloyl to fabricate an inverse opal structure, demonstrating the feasibility of our approach to engineer the alveolar lung model using different hydrogel biomaterials (*SI Appendix*, Fig. S3).

The structure (all based on GelMA below) was further characterized by scanning electron microscopy, as illustrated in Fig. 2 *A*, *ii*, *Inset* and *SI Appendix*, Fig. S4, in which an interconnecting window between two adjacent sacs could be observed. The fluorescence confocal images of the fluorescein isothiocyanate (FITC)-conjugated GelMA before and after alginate microbead removal further verified their structure (Fig. 2 *A*, *iii*).

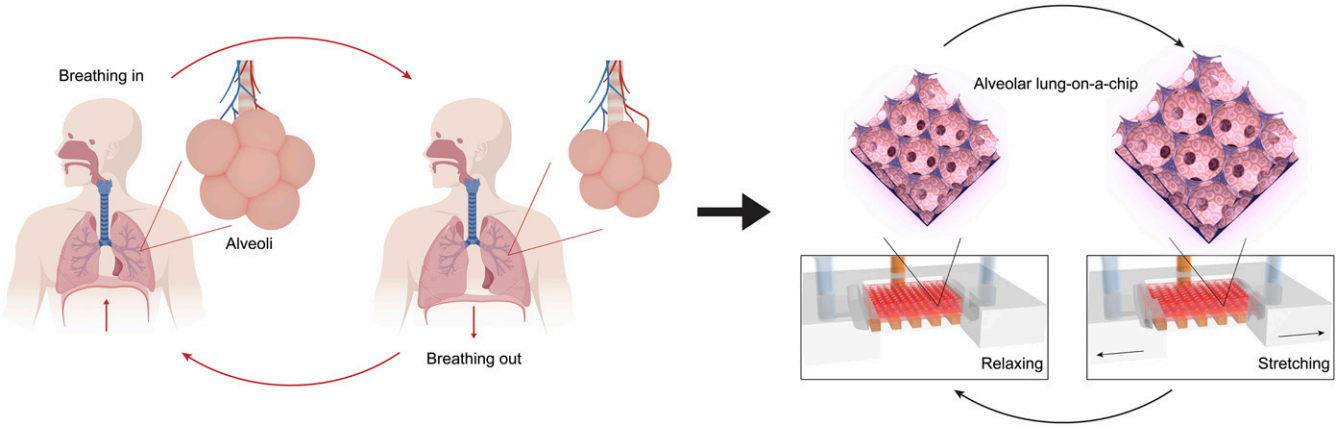

Fig. 1. The breathing human alveolar lung-on-a-chip. Schematics showing the distal lung, the breathing cycles, and the in vitro on-chip model of the breathing alveolar lung.

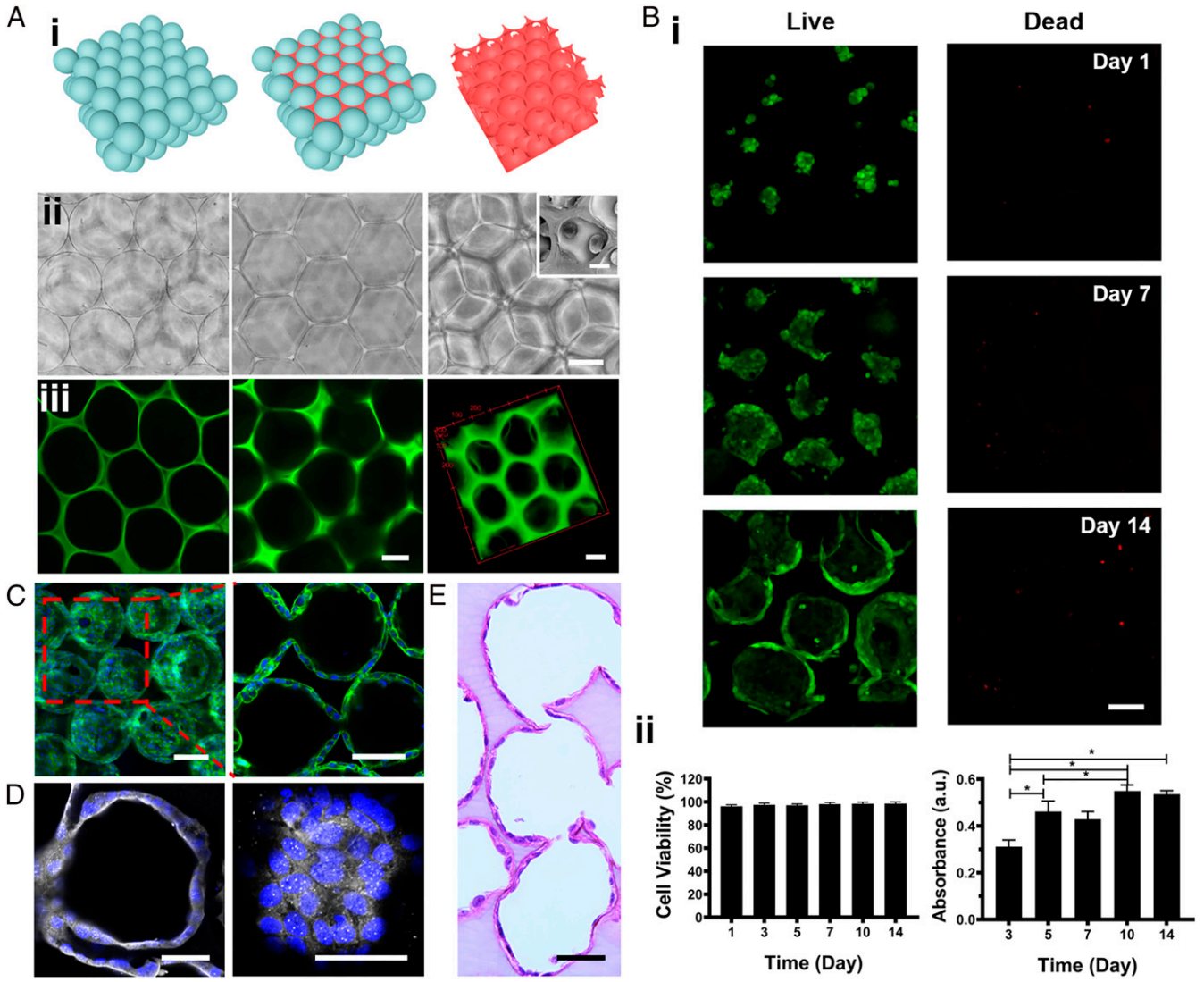

Fig. 2. Fabrication of the alveoli-like 3D GelMA inverse opal structure and formation of the alveolar lung model. (*A*, *i* and *ii*) Schematics and bright-field optical images showing the fabrication process of the alveoli-like 3D GelMA inverse opal structure. Alginate microbeads with uniform sizes (201 ± 12 μm) were first assembled into a cubic close-packed lattice (*Left*); a 7% (wt/wt) GelMA solution was then infiltrated into the void spaces of the lattice and cross-linked (*Center*). Finally, the alginate microbeads were selectively removed using EDTA, leaving behind an alveoli-like hydrogel structure (*Right*). (Scale bar: 100 μm.) *A*, *ii*, *Right*, *Inset* shows an scanning electron microscopy image of the interconnecting window between two adjacent sacs. (Scale bar: 20 μm; note the shrinkage of the sac size comparing to optical images was caused by the sample-drying process for scanning electron microscopy imaging.) (*A*, *iii*) Fluorescence confocal images illustrating the GelMA inverse opal hydrogel structure, where GelMA was chemically labeled with FITC. (*Left*) After infiltration of the GelMA solution into the void spaces of the alginate microbead lattice and cross-linking, (*Center*) after removal of the alginate microbeads, and (*Right*) 3D reconstruction of the GelMA hydrogel structure. (Scale bars: 100 μm.) (*B*, *i*) Fluorescence confocal images showing the hAECs cultured in the GelMA inverse opal hydrogel structures at 1, 7, and 14 d. Green, live cells; red, dead cells. (Scale bar: 100 μm.) (*B*, *ii*) Quantification of viability (*Left*) and proliferation (*Right*) of the hAECs in the GelMA inverse opal hydrogel structures. $*P < 0.05$. (*C*) Confocal reconstruction view (*Left*) and sectional view (*Right*) of the hAECs after culturing for 14 d in the GelMA inverse opal hydrogel structure, in which the fully confluent alveolar epithelium was formed. Green, F-actin; blue, nuclei. (Scale bars: 100 μm.) (*D*) Confocal micrographs showing the presence of continuous tight junctions of the rim (*Left*) and bottom (*Right*) of a sac after culturing for 14 d in the GelMA inverse opal hydrogel structure. White, ZO-1; blue, nuclei. (Scale bars: 50 μm.) (*E*) Representative image of an H&E-stained section of the alveolar lung model after 14 d of culture. (Scale bar: 50 μm.)

The alginate microbeads were prepared by electrospraying the alginate solution into a $CaCl_2$ solution for immediate physical cross-linking (*SI Appendix*, Fig. S5). The influence of each parameter, including alginate concentration, voltage, needle diameter, flow rate, and ring diameter, on the formation of the microbeads was carefully studied (*SI Appendix*, Figs. S6–S10). While a wide range of diameters could be conveniently achieved, uniform alginate microbeads measuring ∼200 μm (201 ± 12 μm) were selected for constructing the alveolar lung model since the average size of each alveolus is ∼200 μm in diameter in the native lung (33). Approximately 7,050 microbeads were packed into three layers, resulting in a roughly 546.4-μm-thick inverse opal structure. Such an inverse opal structure represented the miniature alveolar lung model that featured the sac-like pores and the interconnecting windows between the sacs, which resembles the native human counterpart in both architecture and dimensions, meaning that the two would also share the same unit surface area. The dimension of the overall 3D GelMA scaffold was 8 × 10 × 3 mm that comprised a layer of bulk GelMA base below the 546.4-μm-thick inverse opal GelMA layer for improved stability.

It should be noted that, although the human alveoli are not necessarily homogeneous in size, in our model we pursued the use of only uniform alginate microbeads as the sacrificial templates to avoid unwanted interferences caused by the heterogeneity in the alveolar sizes. Indeed, we have previously demonstrated that the use of porous scaffolds with uniform pores is experimentally superior to those with random pores even if the average pore size falls in the same range (20, 21). In fact, we were also able to fabricate the 3D inverse opal GelMA structures with different yet uniform pore sizes using monodispersed alginate microbeads of different diameters. The microbeads with sizes of 325.9 ± 10.5, 199.6 ± 1.1, and 156.3 ± 2.7 μm were used separately to fabricate 3D GelMA structures with corresponding pore sizes (*SI Appendix*, Fig. S11). Likewise, we could also fabricate a 3D GelMA structure with heterogeneous pore sizes by using randomly mixed microbeads with three diameters (~200, ~250, and ~300 μm) as the template (*SI Appendix*, Fig. S12). The alginate microbeads could be rapidly removed by treating with the 0.01 M EDTA solution. The complete removal of the alginate microbeads from the scaffold was confirmed by both scanning electron microscopy imaging and X-ray energy dispersive spectroscopy (EDS) mapping, shown in *SI Appendix*, Fig. S13. In particular, EDS mapping profiles suggested that while 1.3% of Ca^{2+} was detected in the sample before removal of the microbeads, no Ca^{2+} (0%) was measured at all after the removal. Thus, removal of both Ca^{2+} and the alginate microbeads was complete.

To model the alveolar epithelium, we populated hAECs on the surfaces of the sacs within the GelMA inverse opal structures. Fluorescence confocal images revealed that the hAECs were almost rounded and crowded at day 1 postseeding, where they were able to gradually spread and proliferate during the following days, eventually covering the full surface areas of the alveoli-like sacs (Fig. 2 *B*, *i* and *C* and *SI Appendix*, Figs. S14 and S15). The viability of the hAECs on the surfaces of the pores in the porous GelMA structures was observed to exceed 95% (Fig. 2*B*). The proliferation of the cells was steady during the first 10 d of culture and slightly slowed down afterward (Fig. 2 *B*, *ii*), possibly due to the contact inhibition upon confluency of the cells on the surfaces of the pores. The cell viability, proliferation, and spreading at the different depths within a single layer of the sacs of the inverse opal structure are shown in *SI Appendix*, Fig. S14. Indeed, fluorescence confocal images suggested that these culture conditions resulted in the formation of a confluent alveolar epithelium (Fig. 2, Movie S1, and *SI Appendix*, Figs. S14 and S15). Significantly, the hAECs were linked by a continuous presence of tight junctions as indicated by Zonula occludens (ZO)-1 staining (Fig. 2*D*). Furthermore, hematoxylin and eosin (H&E) staining provided an overview of the structure of the GelMA hydrogel and the cell distributions, clearly validating the emulation of the alveoli-like, interconnected sacs and the continuous monolayer of hAECs on the pore surfaces (Fig. 2*E*).

Comparisons between 2D and 3D Cultures of the Human Alveolar Epithelium. Reconstitution of the 3D structures and microenvironments of the tissues is vital for realizing their functions and modeling pathophysiology in vitro (34, 35). To investigate the advantages of our 3D GelMA inverse opal structures in the recapitulation of the pulmonary alveoli, the behaviors of hAECs were carefully compared with those cultured on 2D GelMA surfaces. The morphologies of the hAECs were further studied by capturing scanning electron microscopy images (Fig. 3*A*) of the cells cultured on both the 3D GelMA structures (Fig. 3 *A*, *Upper*) and the 2D GelMA surfaces (Fig. 3 *A*, *Lower*) at days 3, 7, and 14. Comparing with the slightly crowded and oftentimes locally aggregated hAECs on the 2D GelMA surfaces during the culture, the hAECs in the 3D GelMA structures appeared to be flatter, where the formation of a smooth, confluent epithelium by well-spread cells was apparent at day 14. The microscopic images of hAECs cultured on the 2D GelMA surfaces are shown in *SI Appendix*, Fig. S16. Moreover, the apparent proliferation rate of the hAECs in the 3D GelMA structures was significantly higher than that of the cells on the 2D surfaces (*SI Appendix*, Fig. S17). Nevertheless, when normalized (Fig. 3*B*), there were no significant differences between the two configurations anymore during the culture period of 10 d. The hAECs in the 3D GelMA structures became higher in numbers than those on the 2D surfaces at day 14, most likely due to the presence of the larger total surface area within the 3D GelMA structure as compared with the 2D surface, at ~2 cm^2 in the former vs. 0.8 cm^2 for the latter despite that they share the same planar size of 8 × 10 mm. Most importantly, the 3D GelMA scaffolds provided an optimal geometry and microarchitecture for cell spreading and proliferation compared with the planar surfaces, which possibly promoted the cellular process such as adhesion, proliferation, and migration. These observations indicated that the 3D culture provided an optimal geometry for cell spreading and proliferation compared with the planar culture when both substrate materials were the same GelMA with similar local mechanical properties, both close to that of the normal human lung tissue (29).

Apoptosis is a fundamental cellular process that is necessary for the maintenance of tissue homeostasis in adult organisms (36). The apoptotic activities of the cells were analyzed via caspase-3/7 staining of hAECs and flow cytometry analyses of annexin V-FITC– and propidium iodide (PI)-stained hAECs both on 2D GelMA surfaces and in 3D GelMA structures. Interestingly, it was found that the mean fluorescence intensity of caspase-3/7 was higher for the cells grown on the 2D GelMA surfaces compared with those in the 3D GelMA structures (Fig. 3*C* and *SI Appendix*, Fig. S18). Similarly, the flow cytometry analyses of annexin V-FITC– and PI-stained hAECs at day 14 and day 22 showed that the overall proportion of late apoptotic/necrotic hAECs on the 2D GelMA surfaces was increased over the culture period compared with those in the 3D GelMA structures (Fig. 3*D* and *SI Appendix*, Fig. S19). While the proportions of early apoptotic cells were higher in 3D structures, the proportions of the late apoptotic/necrotic cells were higher on the 2D GelMA surfaces, at both day 14 (Fig. 3*D*) and day 22 (*SI Appendix*, Fig. S19). It is therefore hypothesized that our unique 3D GelMA inverse opal structure resembling that of the human alveoli could possibly provide the cells with an in vivo-like microenvironment, which promoted optimal cell–ECM and cell–cell interactions.

To explore the differentially expressed genes to detect biological changes in hAECs cultured in 2D and 3D, we performed additional transcriptome profiling through gene microarray analyses. Other than the 2D GelMA surfaces, we further included another control group based on the 2D PDMS surfaces (a commonly used substrate in various organ-on-chip models, including those of the lung) to compare with the 3D GelMA structure-based hAEC culture. Scatterplots and the Venn diagram (*SI Appendix*, Fig. S20 *A* and *B*) were generated for the three comparisons (i.e., 3D GelMA vs. 2D PDMS, 3D GelMA vs. 2D GelMA, and 2D GelMA vs. 2D PDMS). We calculated the normalized expression values (fragments per kilobase per million mapped reads) of every gene analyzed in the three groups, and those values with greater than twofold increase or decrease with a false discovery rate of less than 0.05 (q value < 0.05) were considered as the differentially expressed genes.

Interestingly, the 3D GelMA vs. 2D PDMS comparison demonstrated that there were 4,757 differentially expressed genes (2,646 up-regulated and 2,111 down-regulated); for 3D GelMA vs. 2D GelMA, there were 2,396 differentially expressed genes (1,352 up-regulated and 1,044 down-regulated), while for 2D GelMA vs. 2D PDMS, there were 5,175 differentially expressed genes (2,553 up-regulated and 2,622 down-regulated) (*SI Appendix*, Fig. S20*B*). To elucidate the biological processes on the different culture substrates, functional gene ontology (GO) and Kyoto Encyclopedia of Genes and Genomes (KEGG) pathway enrichment analyses

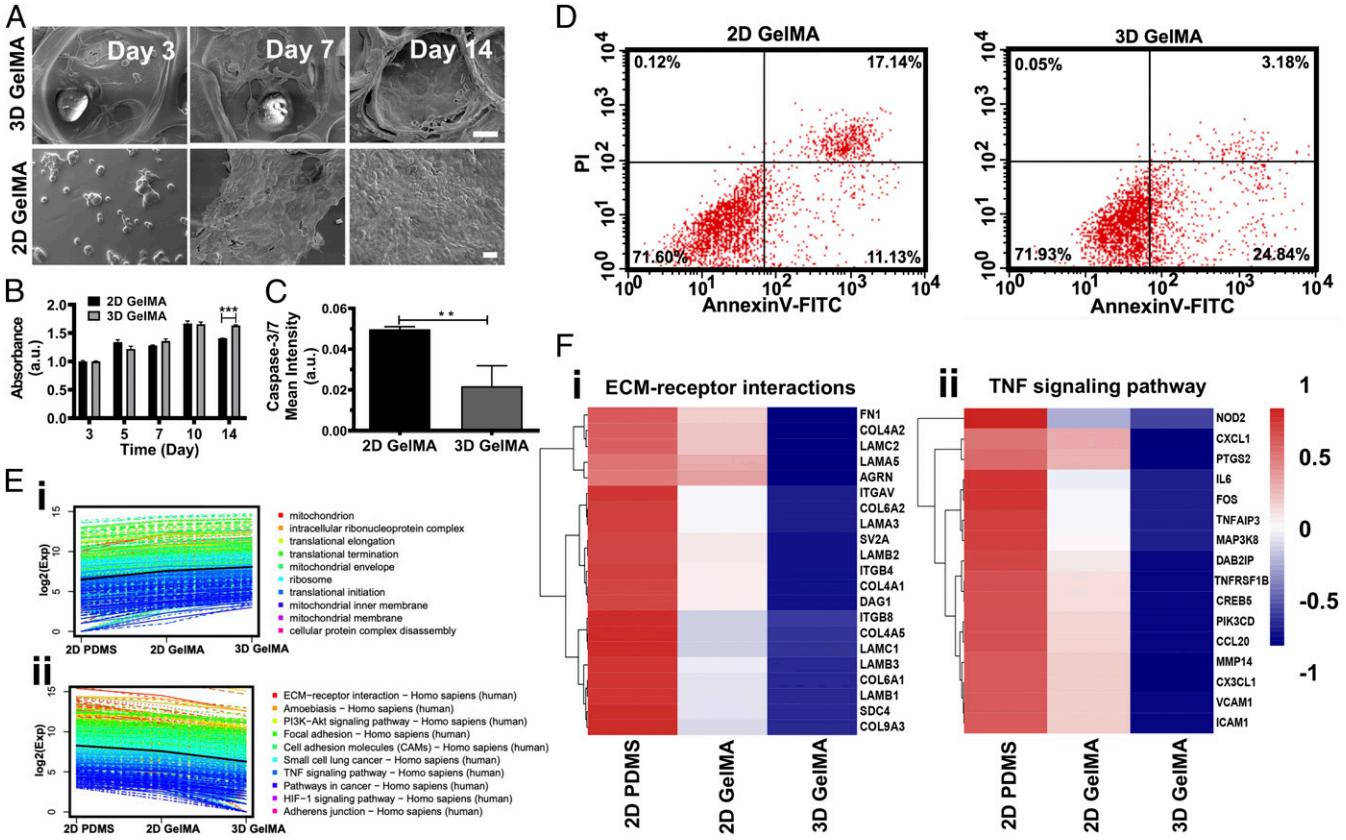

Fig. 3. Comparisons of the alveolar epithelium formation for hAECs cultured on 3D and 2D substrates of GelMA and PDMS. (*A*) Scanning electron microscopy images of the hAECs cultured on/in the 3D GelMA inverse opal structure (*Upper*) and the 2D GelMA hydrogel (*Lower*) at days 3, 7, and 14. (Scale bars: 25 μm.) (*B*) Normalized proliferation of hAECs on the two GelMA surfaces. ***$P < 0.001$. (*C*) Caspase-3/7 fluorescence signal analysis and annexin V-FITC/PI flow cytometry plots of hAECs on the two GelMA surfaces. **$P < 0.01$. (*D*) Flow cytometry analyses of annexin V-FITC– and PI-stained hAECs cells at day 14. (*E*) K-means clusters of the genes for (*i*) GO enrichment and (*ii*) KEGG enrichment analyses of hAECs cultured on 2D PDMS, on 2D GelMA, and in 3D GelMA for 14 d. (*F*) Heat maps showing differential genes expressions relating to (*i*) ECM–receptor interactions and (*ii*) TNF signaling pathway of hAECs cultured on 2D PDMS, on 2D GelMA, and in 3D GelMA for 14 d. a.u.: any unit; PI3K-Akt: phosphatidylinositol 3-kinase-protein kinase B; HIF-1α: hypoxia-inducible factor-α.

were further performed (*SI Appendix*, Fig. S20*C*). Through K-means clustering analysis of the differentially expressed genes in the three groups, heat maps relating to GO and KEGG enrichment analyses of clusters showed similar gene expression trends (Fig. 3*E* and *SI Appendix*, Fig. S20 *D* and *E*).

We have specifically focused on some key functional categories to better understand the major differences for the hAECs cultured on 2D PDMS, 2D GelMA, or 3D GelMA, exhibited as the GO enrichment analysis in Fig. 3 *E*, *i* and KEGG enrichment analysis in Fig. 3 *E*, *ii*. The genes associated with ECM–receptor interactions, focal adhesion, tumor necrosis factor (TNF) signaling pathway, and small-cell lung cancer in the clusters had a monotonically decreasing trend from 2D PDMS and 2D GelMA to 3D GelMA cultures, while oxidative phosphorylation in the cluster showed an increasing trend (*SI Appendix*, Fig. S20). Similarly, biological processes regarding mitochondrial biogenesis also possessed an increasing trend in the order of 2D PDMS, 2D GelMA, and 3D GelMA cultures. Mitochondria provide the cells with adenosine triphosphate through the oxidative phosphorylation activity, and up-regulation of these pathways could provide more energy to help maintain the functionality of the cells (37, 38). Specifically, heat maps were produced to compare differentially expressed genes involved in ECM–receptor interactions and the TNF signaling pathway. Integrin-β4 (*ITGB4*), which is one of the transmembrane receptors for ECM proteins, can form a stable attachment to the basal membrane in polarized epithelial cells through the formation of hemidesmosomes (39) and also has a significant impact on signaling events that stimulate migration and invasion (40). It was observed that the hAECs expressed more *ITGB4* and interleukin-6 (*IL-6*) in 2D conditions (both GelMA and PDMS) than in 3D GelMA (Fig. 3*F*), possibly indicating a response to the more unnatural 2D microenvironments. Focal adhesions are key transducers of outside-in signaling that enable cells to sense cues from the ECM and generate forces (41). In 2D cultures, especially for PDMS, up-regulation of focal adhesion genes and ECM–receptor interaction genes might be caused by the stiff and pathologically activated surfaces (41, 42). Prior studies further reported that TNF-induced death signaling induced alveolar epithelial dysfunction in acute lung injury (43) and also, the increase of IL-6 expression in lungs with diffuse alveolar damage (44, 45). Collectively, these analyses hinted that our 3D GelMA inverse opal structure provided better capabilities to maintain and promote the functions of hAECs in a more in vivo-like manner compared with 2D models, particularly those based on the planar PDMS surfaces.

Construction of a Breathing Human Alveolar Lung-on-a-Chip Model. A schematic diagram of the alveolar lung-on-a-chip (*Upper*) and a photograph of an actual device are shown in Fig. 4*A*. The fabrication process of the chip is schemed in *SI Appendix*, Fig. S21. The chip was composed of the 3D porous GelMA inverse opal scaffold (red part in the schematic) bonded to a PDMS chip. The PDMS support was designed to provide the 3D hydrogel with the medium supply and cyclic mechanical actuations. The medium supply was

realized by slowly infusing the medium through the open channels at the bottom of the PDMS chip. The cyclic mechanical movements were applied to the 3D hydrogel via applying the programmed negative pressures to the two side chambers at the frequency of 0.2 Hz (the normal breath frequency of human).

The mechanical movements of the chip allowed the airflow in and out of the embedded 3D GelMA structure. There are some reports that have focused on building and simulating the airflow in the artificial alveoli (46, 47); however, only few successfully reconstituted the 3D structures of the human alveolar sacs. Herein, we demonstrated the airflow in and out of the alveoli-like structure in our inverse opal alveolar lung model during a breathing cycle, as shown in the simulation results in *SI Appendix*, Fig. S22 *A*, *C*, and *E* as well as in Movie S2. During the "breathing" of the chip, the air gradually flowed into and then out of the inverse opal sacs spontaneously due to the volume change-induced pressure variation with velocity values and Reynolds numbers (0.71 to 1.70), which are very similar to those found in the real human alveoli. In addition, direction of the airflow changed according to the structural framework within the inverse opal alveolar lung model, especially in correspondence at the "alveolus–alveolus" interfaces. On the contrary, in the control 2D model, the airflow followed nonphysiological straighter paths without showing rapid changes of directions (*SI Appendix*, Fig. S22 *B*, *D*, and *F*).

After seeding the hAECs in the 3D GelMA inverse opal structures in the chips, the cells were cultured for 14 d. Live/dead images revealed that the cell viability remained high after 14 d of static culture in the chips (Fig. 4 *B*, control). When the cyclic stretch was applied, the hAECs grown on the surfaces of the pores could "breathe" along with the cyclic mechanical movements that stretched the GelMA structure, where the average size of alveoli was observed to expand by ~8% from the state of "breath out" to "breath in" (Fig. 4*C* and Movie S3). This value is within the 5 to 15% physiological range of strain experienced by the alveoli in the human lung (10). It was, in fact, convenient for us to control the strains or breathing frequencies on the chip as needed by varying the size of the two side chambers or the frequency of the negative pressure applied. As shown in Movie S4, our chip-based model functioned well under a range of strain levels of 5, 10, and 15%, as well as breathing frequencies of 0.1, 0.2, 0.4, and 0.8 Hz.

An ALI was also created for the hAECs in the chip by removal of the medium from the sacs and supplying the medium through the parallel channels underneath the GelMA structure at the bottom of the chip. The relatively low thickness (<3 mm) of the GelMA hydrogel and its nano-/microscale porosities were believed to enable efficient medium transport to support cellular functions. To confirm the sufficient supply of nutrients within the top layer of the 3D GelMA inverse opal structure, we assessed the diffusion of both small molecules (FITC) as well as larger molecules (FITC-dextran, M_w = 10 kDa). It was found that the diffusion of both types of molecules across the entire GelMA structure occurred within relatively short periods (*SI Appendix*,

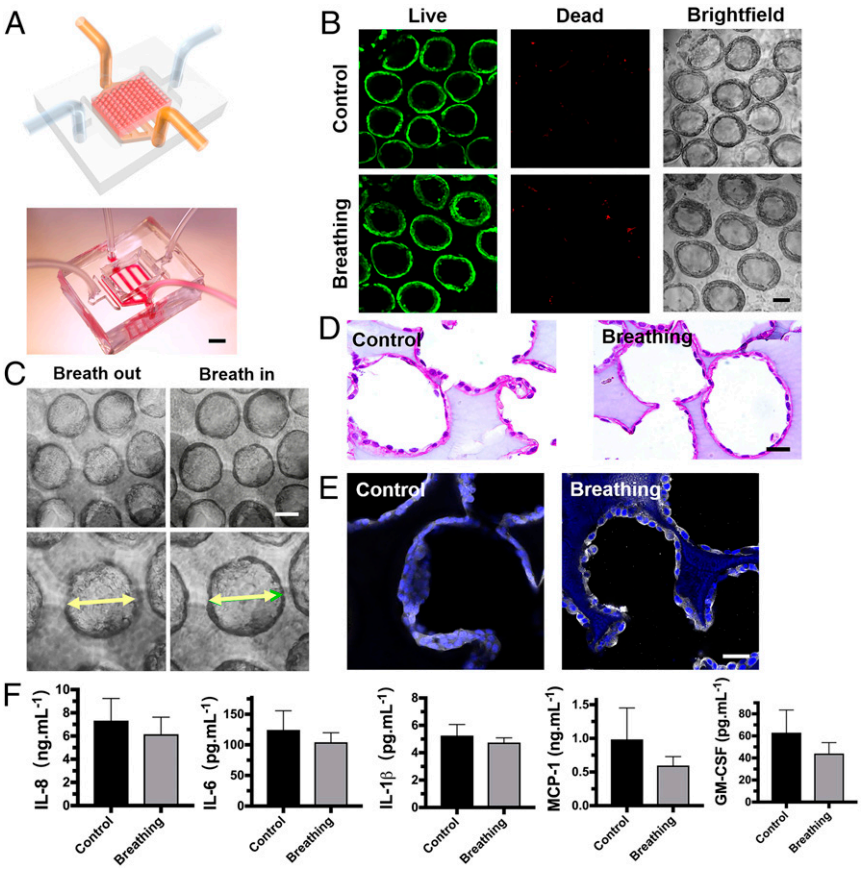

Fig. 4. Construction of the alveolar lung-on-a-chip model. (*A*) Schematic representing the alveolar lung-on-a-chip (*Upper*) and photograph of a device without the GelMA inverse opal structure to show the underlying fluidic channels (*Lower*). (Scale bar: 5 mm.) (*B*) Fluorescence images showing the viability of the hAECs cultured in the chips without and with the breathing events. Green, live cells; red, dead cells. (Scale bar: 100 μm.) (*C*) Micrographs showing the expansion of the sacs under a strain of 8%. (Scale bar: 100 μm.) (*D*) Images of H&E-stained sections showing the epithelium formation in the chips without and with the breathing events. (Scale bar: 50 μm.) (*E*) ZO-1 staining showing the tight junction formation of the epithelium in the chips without and with the breathing events. White, ZO-1; blue, nuclei. (Scale bar: 50 μm.) (*F*) The quantified levels of secreted cytokines IL-8, IL-6, IL-1β, MCP-1, and GM-CSF by hAECs cultured in the chips without and with the breathing events. All analyses were performed at 14 d of culture.

Fig. S23). Since the diffusion is a continuous process, this observation potentially suggested good transport of various components within the culture medium through the GelMA structure.

Indeed, the hAECs cultured within the alveolar lung-on-a-chip devices remained viable after the incorporation of the ALI and the application of the breathing events for 48 h (Fig. 4 *B*, breathing), while the formed alveoli-like epithelial monolayer within the GelMA inverse opal structure could be completely preserved as revealed in the H&E-stained sections (Fig. 4*D*). Moreover, the presence of cyclic mechanical strains seemed to have promoted the formation

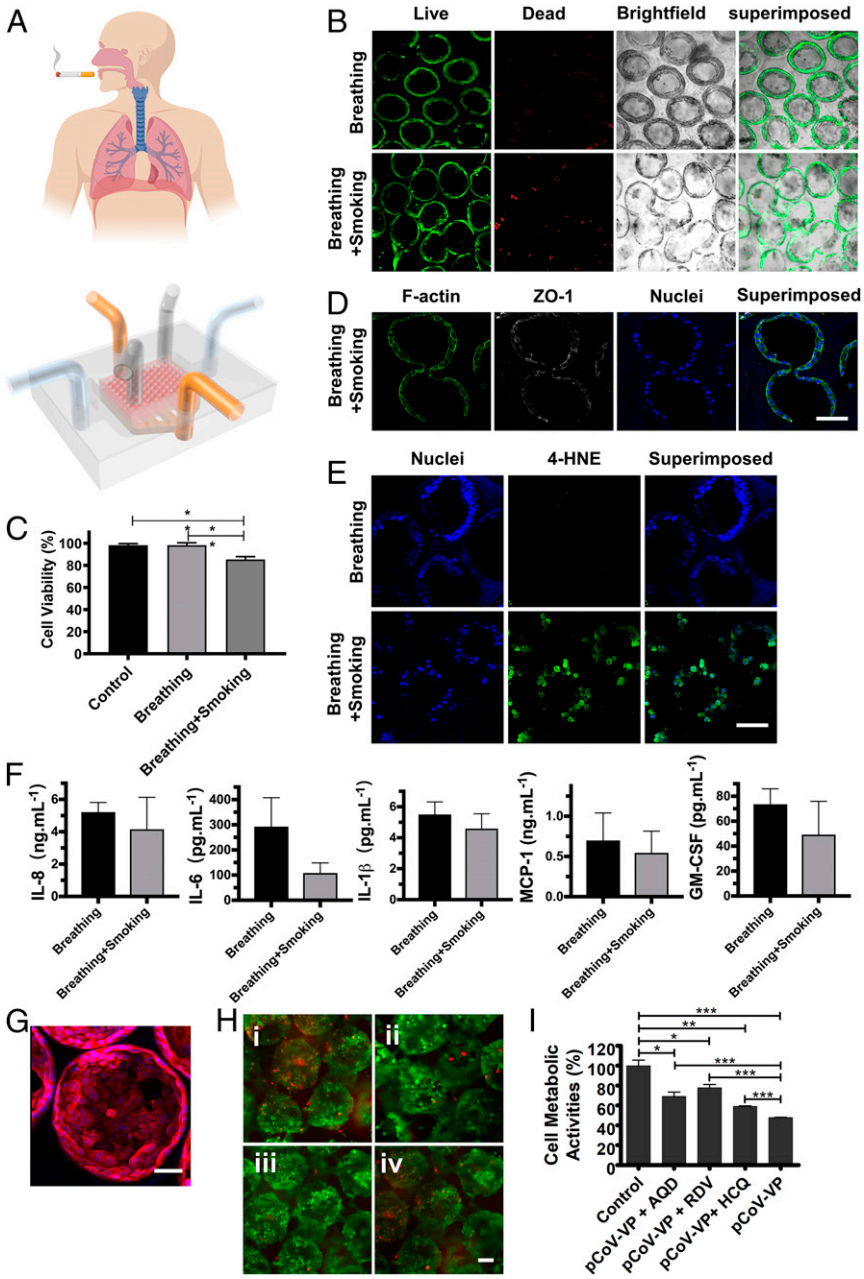

Fig. 5. The effects of smoking and SARS-CoV-2 pseudoviral infection on the alveolar lung-on-chip model. (*A*) Schematic diagrams showing the smoking alveolar lung-on-a-chip. (*B*) Live/dead staining of the hAECs in the alveolar lung-on-a-chip devices before and after smoking. Green, live cells; red, dead cells. (Scale bar: 100 μm.) (*C*) Quantification of cell viability for hAECs. Control: without breathing and smoking; breathing: with breathing but without smoking; and breathing + smoking: with breathing and smoking. (*D*) Confocal fluorescence images showing the effects of smoking on tight junctions of the alveolar epithelium, revealed by ZO-1 staining. White, ZO-1; blue, nuclei. (Scale bar: 100 μm.) (*E*) Confocal fluorescence images showing induction of oxidative stress with smoking. Green: 4-HNE; blue, nuclei. (Scale bar: 100 μm.) (*F*) The quantified levels of secreted cytokines IL-8, IL-6, IL-1β, MCP-1, and GM-CSF by hAECs cultured in the chips. All analyses were performed at 14 d of culture, and smoking was conducted for 75 min. (*G*) Fluorescence confocal images showing the expression of ACE2 receptors by hAECs in the GelMA inverse opal structures at day 14. Red, ACE2 receptors; blue, nuclei. (Scale bar: 50 μm.) (*H*) Fluorescence microscopic images showing the live/dead staining for hAECs in the GelMA inverse opal structures after (*i*) pCoV-VP infection without antiviral drugs, (*ii*) pCoV-VP infection in the presence of amodiaquine (5 μM), (*iii*) pCoV-VP infection in the presence of remdesivir (10 μM), and (*iv*) pCoV-VP infection in the presence of hydroxychloroquine (40 μM). Green, live cells; red, dead cells. (Scale bar: 100 μm.) (*I*) MTS assay showing metabolic activities of hAECs in the GelMA inverse opal structures after pCoV-VP infection in the absence and presence of antiviral drugs. $*P < 0.05$; $**P < 0.01$; $***P < 0.001$.

of tight junctions, indicated by ZO-1 staining (Fig. 4*E*) (48). The levels of secreted cytokines including IL-8, IL-6, IL-1β, monocyte chemoattractant protein-1 (MCP-1), and granulocyte-macrophage colony-stimulating factor (GM-CSF) were further profiled; they were all slightly reduced upon breathing stimulation, yet no significant differences could be found (Fig. 4*F*).

Analysis of Cigarette Smoking Effects on the Alveolar Lung-on-a-Chip Model. Cigarette smoking is one of the major factors leading to the development of COPD, currently the third leading cause of chronic morbidity and mortality worldwide (2, 49, 50), as well as resulting in lung cancer as the most common lethal neoplasm (51). Since the alveolar epithelium is the barrier between the inhaled air and the underlying components (52), the establishment of a smoking alveolar lung-on-a-chip model to examine the distal lung injury and study the effects of smoking on the alveolar epithelium becomes important. While a smoking lung-on-a-chip platform was previously demonstrated using airway epithelial cells on a synthetic polyethylene terephthalate membrane (53), no model currently exists for the distal lung (i.e., the alveoli). Our smoking alveolar lung-on-a-chip model consisted of a smoking device (53, 54) and an additional compartment on top of the breathing alveolar lung-on-a-chip platform to mimic the airway–alveoli transport route (Fig. 5*A*). After smoking ∼10 cigarettes and further culturing for 24 h, dead cells within our alveoli model showed an increase (Fig. 5*B*), and the viability of hAECs was significantly decreased compared with normal breathing and control groups (Fig. 5*C*). The apoptotic activities of the cells before and after the application of the cigarette smoke were analyzed via caspase-3/7 staining of hAECs on/in both 2D and 3D scaffolds (*SI Appendix*, Fig. S24). Consistent with the cultures without the chips (Fig. 3*C* and *SI Appendix*, Fig. S18), hAECs on 2D GelMA in the chip also showed a higher apoptotic tendency (*SI Appendix*, Fig. S24*A*) as compared with those in 3D GelMA structures (*SI Appendix*, Fig. S23*B*). The smoking further resulted in the increase of apoptosis of hAECs in both configurations (*SI Appendix*, Fig. S24 *A–C*). This observation was, in addition, reflected in cellular activity assay (*SI Appendix*, Fig. S24*D*).

In addition, the tight junctions between the hAECs were partially damaged after smoking (Fig. 5*D*). The oxidants in cigarette smoke can induce cellular injuries (55), where 4-hydroxy-2-nonenal (4-hydroxynonenal [4-HNE]) is a major product of lipid peroxidation and a marker of oxidative stress (56, 57). 4-HNE can react with DNAs and proteins to produce various adducts that can lead to cell apoptosis, and the 4-HNE expression level in the alveolar epithelium is negatively correlated with pulmonary functions and contributes to the pathogenesis of various pathological manifestations such as COPD (58). Our results indicated an elevation in the intensity of nuclear 4-HNE staining postsmoking (Fig. 5*E*), and such a high expression of 4-HNE may further induce downstream cellular damage. As a result, the soluble cytokine levels of IL-8, IL-6, IL-1β, MCP-1, and GM-CSF after smoking slightly declined compared with the normal breathing group, suggesting that the functions of hAECs to inhibit proinflammatory responses were compromised when they were exposed to cigarette smoke, consistent with literature (53).

Analysis of SARS-CoV-2 Pseudoviral Infection and Treatment Efficacies on the Alveolar Lung-on-a-Chip Model. COVID-19 caused by SARS-CoV-2 has led to a global public health crisis and is associated with high mortality, mostly caused by acute respiratory distress syndrome (59, 60). As the lungs are the first body organ affected by COVID-19, we further assessed the applicability of our alveolar lung-on-a-chip to investigate SARS-CoV-2 pseudoviral infection. In addition, the antiviral efficacies of two clinically approved antiviral drugs, remdesivir (61) and hydroxychloroquine (62), as well as an antimalarial drug, amodiaquine (63), were evaluated. The latter has also been given to individuals infected with SARS-CoV-2 (64). Since it has been well recognized that SARS-CoV-2 uses angiotensin converting enzyme 2 (ACE2) as a receptor for cellular entry, prior to SARS-CoV-2 pseudoviral particle (pCoV-VP) infection on the alveolar lung-on-a-chip, we first detected the expression of ACE2 receptors by hAECs grown on the surfaces of the alveolar sacs. The hAECs showed a higher level of expression of ACE2 receptors as shown in Fig. 5*G* and *SI Appendix*, Fig. S25*A*. The chips were then inoculated with pCoV-VPs at multiplicity of infection (MOI) of 0.5 for 48 h to identify the virus susceptibility in vitro in the presence and absence of antiviral drugs. At 48 h postinfection, the infection of hAECs with mcherry-labeled pCoV-VPs was observed under a fluorescence microscope (*SI Appendix*, Fig. S25*B*), and cytopathic effect of pCoV-VPs was assessed by live/dead assay (Fig. 5*H* and *SI Appendix*, Fig. S25*C*) and 3-(4,5-dimethylthiazol-2-yl)-5-(3-carboxymethoxyphenyl)-2-(4-sulfophenyl)-2H-tetrazolium (MTS) assay (Fig. 5*I*). The results showed that the cytopathic effects of pCoV-VPs were decreased by approximately 21.4, 30.0, and 11.3% at 5 μM amodiaquine, 10 μM remdesivir, and 40 μM hydroxychloroquine, respectively (Fig. 5*I*). Thus, these drugs significantly inhibited the infection-induced hAEC death by the SARS-CoV-2 pseudotyped viral particles expressing the SARS-CoV-2 spike proteins in our alveolar lung-on-a-chip.

Conclusions and Perspectives

This study provided an example of recreating the architecturally relevant alveolar lung-on-a-chip model and demonstrated its structural and functional features. We have successfully reconstructed some of the key aspects of the human pulmonary alveoli, including the microarchitecture, the ECM microenvironment, the ALI, and the mechanical breathing events. The alveolus in the lung is one of the most important structural determinants of the architecture of the respiratory parenchyma and lung functions. Our breathing alveolar lung-on-a-chip model could broadly reproduce the 3D anatomical structures and functions of the alveoli through the use of a precisely defined 3D porous GelMA hydrogel based on an inverse opal structure, while the breathing function was realized by situating the hAEC-populated GelMA structure in PDMS chip device. Based upon the breathing alveolar lung-on-chip model, we subsequently built a cigarette-smoking alveolar lung-on-a-chip platform, where the negative effects of smoking on the hAECs could be readily explored. We further demonstrated the applicability of our alveolar lung model for investigating SARS-CoV-2 pseudoviral infection and treatment efficacies of antiviral drugs such as hydroxychloroquine, remdesivir, and amodiaquine. While remdesivir and amodiaquine have been approved by the Food and Drug Administration to treat COVID-19 (64), in vitro and in vivo studies have shown the discrepancies in antiviral activity of hydroxychloroquine against SARS-CoV-2 (62).

We have also showcased the possibility of creating the alveolar–capillary interface, which is another key microstructure in the human distal lung that enables the gas exchange in the alveoli by incorporating the human umbilical vein endothelial cells into the matrix of the GelMA inverse opal hydrogel to form the microvascular network surrounding the sacs (*SI Appendix*, Fig. S26). In addition, to investigate the capability of our strategy to reconstitute pathological models of the lung or in particular, lung cancer, we also built a nonsmall-cell lung cancer model with A549 cells. As shown in *SI Appendix*, Fig. S27, the A549 cells could form a good alveolar structure in our platform with good cell viability and morphologies (note the multilayered growth of the A549 cells in some regions in comparison with the monolayer epithelium formed by normal hAECs).

Although surfactant lining layer at the ALI is extremely important for maintaining the alveolar functions, hAECs that we used in this study were commercially sourced, where the vendor unfortunately did not provide any information on AEC types I/II.

It would be indeed very interesting for us in our future work to introduce defined populations of hAECs in our model, to study their effects on alveolar functions and pathologies such as infections.

While our system has some limitations, this example of the miniature alveolar lung-on-a-chip platform provides the foundation and can be readily expanded in the future to provide full functionality of the alveolar units in vitro to provide a niche for lung and lung disease modeling and research.

Methods

SI Appendix, Supplementary Text has detailed experimental procedures that describe the 1) synthesis of alginate microbeads; 2) synthesis of GelMA; 3) fabrication of GelMA inverse opal structures; 4) fabrication of the GelMA inverse opal structure-embedded chip device; 5) fabrication of the smoking device; 6) cell culture in 3D GelMA inverse opal structures; 7) cell culture on 2D GelMA surfaces; 8) construction of the alveolar lung-on-a-chip; 9) cellular characterizations; 10) scanning electron microscopy imaging; 11) apoptosis analyses; 12) microarray analyses; 13) analysis of chemokines and cytokines; 14) computational simulations; 15) SARS-CoV-2 pseudotyped virus production and infection of the alveolar lung-on-a-chip; and 16) statistical analyses.

Data Availability. All study data are included in the article and/or supporting information.

ACKNOWLEDGMENTS. This work was supported by the Brigham Research Institute, the New England Anti-Vivisection Society (NEAVS), and the American Fund for Alternatives to Animal Research (AFAAR). D.H. acknowledges support from National Natural Science Foundation of China Grants 11502158 and 11632013 and Shanxi Provincial Key Research and Development Project, China Grant 201803D421060. A.M.G. acknowledges support from the European Union's Horizon2020 Research and Innovation Program under Grant 760921 (PANBioRA: Personalised and Generalised Integrated Biomaterial Risk Assessment). We also thank Junjie Lv for sharing molecular biology tools at the early stage of the project.

1. A. Papi, C. Brightling, S. E. Pedersen, H. K. Reddel, Asthma. *Lancet* **391**, 783–800 (2018).
2. J. L. López-Campos, W. Tan, J. B. Soriano, Global burden of COPD. *Respirology* **21**, 14–23 (2016).
3. F. Krammer *et al*., Influenza. *Nat. Rev. Dis. Primers* **4**, 3 (2018).
4. L. A. Mandell, M. S. Niederman, Aspiration pneumonia. *N. Engl. J. Med.* **380**, 651–663 (2019).
5. M. J. A. Reid *et al*., Building a tuberculosis-free world: The Lancet Commission on tuberculosis. *Lancet* **393**, 1331–1384 (2019).
6. R. S. Herbst, D. Morgensztern, C. Boshoff, The biology and management of non-small cell lung cancer. *Nature* **553**, 446–454 (2018).
7. World Health Organization, "Coronavirus disease (COVID-2019) situation reports" (Rep. No. 36, World Health Organization, Geneva, Switzerland, 2020).
8. P. N. Fonkwo, Pricing infectious disease. The economic and health implications of infectious diseases. *EMBO Rep.* **9** (suppl. 1), S13–S17 (2008).
9. A. Akhtar, The flaws and human harms of animal experimentation. *Camb. Q. Healthc. Ethics* **24**, 407–419 (2015).
10. D. Huh *et al*., Reconstituting organ-level lung functions on a chip. *Science* **328**, 1662–1668 (2010).
11. D. Huh *et al*., Acoustically detectable cellular-level lung injury induced by fluid mechanical stresses in microfluidic airway systems. *Proc. Natl. Acad. Sci. U.S.A.* **104**, 18886–18891 (2007).
12. W. W. Hope *et al*., Pathogenesis of *Aspergillus fumigatus* and the kinetics of galactomannan in an in vitro model of early invasive pulmonary aspergillosis: Implications for antifungal therapy. *J. Infect. Dis.* **195**, 455–466 (2007).
13. D. D. Nalayanda *et al*., An open-access microfluidic model for lung-specific functional studies at an air-liquid interface. *Biomed. Microdevices* **11**, 1081–1089 (2009).
14. L. Gregson, W. W. Hope, S. J. Howard, In vitro model of invasive pulmonary aspergillosis in the human alveolus. *Methods Mol. Biol.* **845**, 361–367 (2012).
15. M. M. Stevens, J. H. George, Exploring and engineering the cell surface interface. *Science* **310**, 1135–1138 (2005).
16. B. Haefeli-Bleuer, E. R. Weibel, Morphometry of the human pulmonary acinus. *Anat. Rec.* **220**, 401–414 (1988).
17. A. Tsuda *et al*., Finite element 3D reconstruction of the pulmonary acinus imaged by synchrotron X-ray tomography. *J. Appl. Physiol.* **105**, 964–976 (2008).
18. L. Knudsen, M. Ochs, The micromechanics of lung alveoli: Structure and function of surfactant and tissue components. *Histochem. Cell Biol.* **150**, 661–676 (2018).
19. B. Grigoryan *et al*., Multivascular networks and functional intravascular topologies within biocompatible hydrogels. *Science* **364**, 458–464 (2019).
20. S.-W. Choi, Y. Zhang, Y. Xia, Three-dimensional scaffolds for tissue engineering: The importance of uniformity in pore size and structure. *Langmuir* **26**, 19001–19006 (2010).
21. Y. Zhang, S.-W. Choi, Y. Xia, Modifying the pores of an inverse opal scaffold with chitosan microstructures for truly three-dimensional cell culture. *Macromol. Rapid Commun.* **33**, 296–301 (2012).
22. S. W. Choi, Y. Zhang, M. R. Macewan, Y. Xia, Neovascularization in biodegradable inverse opal scaffolds with uniform and precisely controlled pore sizes. *Adv. Healthc. Mater.* **2**, 145–154 (2013).
23. Y. S. Zhang, K. P. Regan, Y. Xia, Controlling the pore sizes and related properties of inverse opal scaffolds for tissue engineering applications. *Macromol. Rapid Commun.* **34**, 485–491 (2013).
24. Y. S. Zhang, C. Zhu, Y. Xia, Inverse opal scaffolds and their biomedical applications. *Adv. Mater.* **29**, 1701115 (2017).
25. J. Lee, N. A. Kotov, Notch ligand presenting acellular 3D microenvironments for ex vivo human hematopoietic stem-cell culture made by layer-by-layer assembly. *Small* **5**, 1008–1013 (2009).
26. J. Lee, G. D. Lilly, R. C. Doty, P. Podsiadlo, N. A. Kotov, In vitro toxicity testing of nanoparticles in 3D cell culture. *Small* **5**, 1213–1221 (2009).
27. M. J. Cuddihy, Y. Wang, C. Machi, J. H. Bahng, N. A. Kotov, Replication of bone marrow differentiation niche: Comparative evaluation of different three-dimensional matrices. *Small* **9**, 1008–1015 (2013).
28. J. Kim, S. A. Bencherif, W. A. Li, D. J. Mooney, Cell-friendly inverse opal-like hydrogels for a spatially separated co-culture system. *Macromol. Rapid Commun.* **35**, 1578–1586 (2014).
29. S. S. Htwe *et al*., Role of Rho-associated coiled-coil forming kinase isoforms in regulation of stiffness-induced myofibroblast differentiation in lung fibrosis. *Am. J. Respir. Cell Mol. Biol.* **56**, 772–783 (2017).
30. K. Yue *et al*., Structural analysis of photocrosslinkable methacryloyl-modified protein derivatives. *Biomaterials* **139**, 163–171 (2017).
31. D. Sicard *et al*., Aging and anatomical variations in lung tissue stiffness. *Am. J. Physiol. Lung Cell. Mol. Physiol.* **314**, L946–L955 (2018).
32. S. R. Polio *et al*., Cross-platform mechanical characterization of lung tissue. *PLoS One* **13**, e0204765 (2018).
33. M. Ochs *et al*., The number of alveoli in the human lung. *Am. J. Respir. Crit. Care Med.* **169**, 120–124 (2004).
34. M. P. Lutolf, J. A. Hubbell, Synthetic biomaterials as instructive extracellular microenvironments for morphogenesis in tissue engineering. *Nat. Biotechnol.* **23**, 47–55 (2005).
35. B. M. Baker, C. S. Chen, Deconstructing the third dimension: How 3D culture microenvironments alter cellular cues. *J. Cell Sci.* **125**, 3015–3024 (2012).
36. F. H. Igney, P. H. Krammer, Death and anti-death: Tumour resistance to apoptosis. *Nat. Rev. Cancer* **2**, 277–288 (2002).
37. A. M. D'Erchia *et al*., Tissue-specific mtDNA abundance from exome data and its correlation with mitochondrial transcription, mass and respiratory activity. *Mitochondrion* **20**, 13–21 (2015).
38. A. A. A. Adam *et al*., AMC-Bio-Artificial Liver culturing enhances mitochondrial biogenesis in human liver cell lines: The role of oxygen, medium perfusion and 3D configuration. *Mitochondrion* **39**, 30–42 (2018).
39. R. O. Hynes, Integrins: Bidirectional, allosteric signaling machines. *Cell* **110**, 673–687 (2002).
40. A. M. Mercurio, I. Rabinovitz, L. M. Shaw, The alpha 6 beta 4 integrin and epithelial cell migration. *Curr. Opin. Cell Biol.* **13**, 541–545 (2001).
41. K. M. Mabry, S. Z. Payne, K. S. Anseth, Microarray analyses to quantify advantages of 2D and 3D hydrogel culture systems in maintaining the native valvular interstitial cell phenotype. *Biomaterials* **74**, 31–41 (2016).
42. V. Petit, J. P. Thiery, Focal adhesions: Structure and dynamics. *Biol. Cell* **92**, 477–494 (2000).
43. B. V. Patel, M. R. Wilson, K. P. O'Dea, M. Takata, TNF-induced death signaling triggers alveolar epithelial dysfunction in acute lung injury. *J. Immunol.* **190**, 4274–4282 (2013).
44. H. Schütte *et al*., Bronchoalveolar and systemic cytokine profiles in patients with ARDS, severe pneumonia and cardiogenic pulmonary oedema. *Eur. Respir. J.* **9**, 1858–1867 (1996).
45. J. Ben-Ari *et al*., Cytokine response during hyperoxia: Sequential production of pulmonary tumor necrosis factor and interleukin-6 in neonatal rats. *Isr. Med. Assoc. J.* **2**, 365–369 (2000).
46. R. Fishler, P. Hofemeier, Y. Etzion, Y. Dubowski, J. Sznitman, Particle dynamics and deposition in true-scale pulmonary acinar models. *Sci. Rep.* **5**, 14071 (2015).
47. R. Fishler, M. K. Mulligan, J. Sznitman, Acinus-on-a-chip: A microfluidic platform for pulmonary acinar flows. *J. Biomech.* **46**, 2817–2823 (2013).
48. K. H. Benam *et al*., Small airway-on-a-chip enables analysis of human lung inflammation and drug responses in vitro. *Nat. Methods* **13**, 151–157 (2016).
49. B. R. Celli, J. A. Wedzicha, Update on clinical aspects of chronic obstructive pulmonary disease. *N. Engl. J. Med.* **381**, 1257–1266 (2019).
50. S. I. Rennard, M. B. Drummond, Early chronic obstructive pulmonary disease: Definition, assessment, and prevention. *Lancet* **385**, 1778–1788 (2015).
51. Forum of International Respiratory Societies, *The Global Impact of Respiratory Disease* (European Respiratory Society, Sheffield, United Kingdom, ed. 2, 2017).
52. M. A. Matthay, L. Robriquet, X. Fang, Alveolar epithelium: Role in lung fluid balance and acute lung injury. *Proc. Am. Thorac. Soc.* **2**, 206–213 (2005).
53. K. H. Benam *et al*., Matched-comparative modeling of normal and diseased human airway responses using a microengineered breathing lung chip. *Cell Syst.* **3**, 456–466.e4 (2016).

54. K. H. Benam, R. Novak, T. C. Ferrante, Y. Choe, D. E. Ingber, Biomimetic smoking robot for in vitro inhalation exposure compatible with microfluidic organ chips. *Nat. Protoc.* **15**, 183–206 (2020).
55. I. Rahman, W. MacNee, Role of oxidants/antioxidants in smoking-induced lung diseases. *Free Radic. Biol. Med.* **21**, 669–681 (1996).
56. M. Breitzig, C. Bhimineni, R. Lockey, N. Kolliputi, 4-Hydroxy-2-nonenal: A critical target in oxidative stress? *Am. J. Physiol. Cell Physiol.* **311**, C537–C543 (2016).
57. A. Ayala, M. F. Muñoz, S. Argüelles, Lipid peroxidation: Production, metabolism, and signaling mechanisms of malondialdehyde and 4-hydroxy-2-nonenal. *Oxid. Med. Cell. Longev.* **2014**, 360438 (2014).
58. I. Rahman *et al*., 4-Hydroxy-2-nonenal, a specific lipid peroxidation product, is elevated in lungs of patients with chronic obstructive pulmonary disease. *Am. J. Respir. Crit. Care Med.* **166**, 490–495 (2002).
59. I.-M. Schaefer *et al*., In situ detection of SARS-CoV-2 in lungs and airways of patients with COVID-19. *Mod. Pathol.* **33**, 2104–2114 (2020).
60. C. L. Onweni *et al*., ACEI/ARB therapy in COVID-19: The double-edged sword of ACE2 and SARS-CoV-2 viral docking. *Crit. Care* **24**, 475 (2020).
61. A. J. Pruijssers *et al*., Remdesivir inhibits SARS-CoV-2 in human lung cells and chimeric SARS-CoV expressing the SARS-CoV-2 RNA polymerase in mice. *Cell Rep.* **32**, 107940 (2020).
62. P. Maisonnasse *et al*., Hydroxychloroquine use against SARS-CoV-2 infection in non-human primates. *Nature* **585**, 584–587 (2020).
63. L. E. DeWald *et al*., In vivo activity of amodiaquine against Ebola virus infection. *Sci. Rep.* **9**, 20199 (2019).
64. S. Weston *et al*., Broad anti-coronavirus activity of food and drug administration-approved drugs against SARS-CoV-2. *J. Virol.* **94**, e01218-20 (2020).